WILEY-VCH

DOI: 10.1002/pssa.201800555
Full Paper

The Role of Graphene-Based Derivative as Interfacial Layer in Graphene/n-Si Schottky Barrier Solar Cells

Andrea Gnisci, Giuliana Faggio, Laura Lancellotti, Giacomo Messina, Riccardo Carotenuto, Eugenia Bobeico, Paola Delli Veneri, Andrea Capasso, Theodoros Dikonimos, Nicola Lisi*

A. Gnisci, G. Faggio, Prof. G. Messina, Prof. R. Carotenuto
Department of Information Engineering, Infrastructures and Sustainable Energy, University "Mediterranea" of Reggio Calabria, Via Graziella, Loc. Feo di Vito, 89124 Reggio Calabria, Italy
E-mail: andrea.gnisci@unirc.it

L. Lancellotti, E. Bobeico, P. Delli Veneri
ENEA, Portici Research Center, P.le E. Fermi 1, 80055 Portici Naples, Italy

A. Capasso
Department of Materials Science and Engineering, Yonsei University, 03722 Seoul, Republic of Korea

N. Lisi, T. Dikonimos
ENEA, DTE PCU IPSE, Casaccia Research Center, Via Anguillarese 301, 00123 Roma, Italy

Keywords: CVD graphene, graphene-based derivative, photovoltaics, solar cell

ABSTRACT: Schottky-barrier solar cells (SBSCs) represent low-cost candidates for photovoltaics applications. The engineering of the interface between absorber and front electrode is crucial for reducing the dark current, blocking the majority carriers injected into the electrode and reducing surface recombination. The presence of tailored interfacial layers between the metal electrode and the semiconductor absorber can improve the cell performance. In this work, we engineered the interface of a graphene/n-type Si SBSC by introducing a graphene-based derivative (GBD) layer meant to reduce the Schottky-barrier height (SBH) and ease the charge collection. The chemical vapor deposition (CVD) parameters are tuned to obtain the two graphene films with different structure and electrical properties: few-layer graphene (FLG) working as transparent conductive electrode and GBD layer with electron-blocking and

hole-transporting properties. Test SBSCs are fabricated to evaluate the effect of the introduction of GBD as interlayer into the FLG/n-Si junction. The GBD layer reduces the recombination at the interface between graphene and n-Si, and improves the external quantum efficiency (EQE) with optical bias from 50 % to 60 %. The FLG/GBD/n-Si cell attains a power conversion efficiency (PCE) of ~5 %, which increase to 6.7 % after a doping treatment by nitric acid vapor.

1. Introduction

In the field of silicon (Si) photovoltaics, Schottky barrier solar cells (SBSCs) based on graphene/n-Si junctions represent an innovative and interesting case study for the integration of two-dimensional materials into consolidated cell architectures and fabrication processes. Graphene and related materials are ideally suited for the fabrication of stacked structures, either in novel device configurations or in conjunction with "classic" photovoltaic (PV) materials. [1] Graphene in the SBSC serves not only as transparent conductive electrode, but can also contribute as an active layer for carrier separation and hole transport. [2–7] This kind of solar cell represent a low-cost and high-efficient alternative to traditional Si solar cells based on p-n junctions. [8–10] In fact, these cells can be fabricated by simply transferring a graphene film onto n-Si substrate at room temperature, making the fabrication process less expensive and easier in comparison to traditional Si solar cells. Power conversion efficiency (PCE) of graphene/n-Si SBSCs passed from 1.5 % [2] to 15.6 % [11] in only five years, by implementing a various kinds of graphene films and optimization strategies: multilayer films, [12,13] chemical doping treatments, [14–18] the introduction of antireflection coatings or light-trapping layers, [16,17,19–21] the engineering of interface between graphene and Si. [11,22–26] Nevertheless, the PCE of these cells are still much lower than that of state-of-the-art crystalline Si solar cells. Interface engineering is crucial in Schottky heterostructures based on graphene, as already reported for graphene/GaAs, [27–30] graphene/InP [31] and graphene/CdTe solar cell. [32–35]. The performance of graphene/n-Si SBSCs is highly affected by the recombination of the charge carriers at the

interface between graphene and Si due to the low Schottky barrier height (~0.6–0.7 eV), much smaller than that of traditional Si solar cells, which causes a large leakage current and thus a low open circuit voltage (V_{oc}). [8] One approach to reduce charge recombination at the interface and improve the performance of the cell consists in engineering the interface by adding interfacial layers. Such layers can play a key role in suppressing the charge recombination and improving the V_{oc} of the cell. A thin native oxide layer (~2 nm) between Si and graphene can act as a passivation layer, reducing the influence of surface defects and reverse dark saturation current, thus improving the Voc. By optimizing the thickness of the native oxide layer a high PCE of 15.6 % has been achieved. [11] The insertion of an insulating layer in the graphene/n-Si junction forms a metal-insulator semiconductor (MIS) structure. [4] In MIS configuration, the additional insulating layer works as an electron blocking layer preventing the diffusion of electrons (majority carriers) from n-Si to graphene and thus reducing the carrier recombination. An appropriate band alignment between the insulating layer and the n-Si can also reduce the effect of hole (minority carrier) transport from n-Si to graphene, but the insulating layer should be uniform and very thin (down to atomic thickness) to avoid increasing the series resistance (R_s). SBSCs with optimized interfacial layers of aluminum oxide (Al_2O_3) [25,36] or hafnium oxide (HfO_2) [26] have been reported to achieve stable, high-efficiency graphene/n-Si junction. 2D materials have been also investigated as interfacial layers: it was reported that MoS_2 monolayer [24,37] and hexagonal boron nitride (h-BN) [29,38] work as effective electron-blocking/hole-transporting layers, and graphene oxide (GO) [23,39] could effectively suppress the interface recombination of graphene/Si solar cells and increase the V_{oc}.

Recently, carbon nanomaterials have been engineered and efficiently introduced in the architecture of innovative PV technology, [40] such as organic [41–44] and perovskite-based solar cells. [45–47] Among the many carbon nanomaterials, graphene-based derivatives [48–51] are particularly relevant in the PV context, given the possibility of fine-tuning their properties (*e.g.*, optical, electronic, mechanical, etc.) according to the device requirements. [52] In the present

work, we report on the use of a graphene based derivative (GBD) made by chemical vapor deposition (CVD) to be used in a SBSC as interfacial layer between few-layer graphene (FLG, acting as transparent conductive electrode) and n-Si (the absorber). Specifically, this GBD is grown by ethanol-CVD at ~ 800° C (i.e., a temperature 200° C lower than the standard one used to grow graphene) [53,54] and as a result its lattice is less crystalline on the long range than pristine graphene and contains heterogeneous groups composed of a mixed phase of sp^2/sp^3-hybridized carbon atoms such as hydrogenated (C−H), carboxyl (C−O−H), or epoxide (C−O−C) bonds. [44] These features reflects in a higher sheet resistance than graphene's, as well as modified UV-vis absorbance and work function. [44] The structural and electronic properties of the GBD were measured by Raman spectroscopy, atomic force microscopy, scanning Kelvin probe and UV-vis absorption spectroscopy. FLG and GBD were integrated into the SBSC architecture by direct transfer of carbon films on Si substrate at room temperature, [55] thus at a lower temperature than the conventional Al_2O_3 or HfO_2 insulating layers deposited by Plasma enhanced chemical vapor deposition (PECVD) at 600°C and Atomic Layer Deposition (ALD) at 200°C. [25,26,36] The GBD, acting as non-conductive hole transport layer, [44] reduces the recombination at the interface and improves the overall cell performance. The devices were tested in dark and light conditions, and the results were compared with a reference solar cell without interfacial layer. FLG/n-Si junction with the GBD interlayer showed a PCE of 4.8 %, associated to an increase of SBH, and a decrease of R_s and ideality constant (η), confirming the reduction of the recombination sites at the interface. A molecular doping treatment (by HNO_3 vapors) was performed on the solar cells with GBD interlayer. The effects of molecular doping on the GBD and, in turn, on the cell performance have been investigated. After the treatment, the cell's PCE increased up to 6.7 %.

2. Experimental Section

2.1. Graphene growth and transfer

Graphene-based films were grown by CVD of ethanol on Cu substrates by varying the process temperature: FLG at 1070 °C and GBD at 790 °C, as previously reported. [44,56] The CVD apparatus consists of a cold-wall chamber, made of a quartz tube equipped with an inductively coupled graphite susceptor heater. The heater is excited by a 3 kW (maximum power) radio frequency current source, which is modulated by the signal of a thermocouple buried inside the graphite susceptor. This configuration presents various advantages over classic CVD system as the reduction of the contamination connected to the quartz tube ageing, [57] fast heating, and a precise control on the process start/end time. After the growth, cyclododecane was used to support the films during the transfer process: [55] the Cu substrate was etched in ammonium persulphate and then the films were rinsed in DI water before they were transferred onto different target substrate for fabrication of the cells and for characterization. After the film transfer, the substrates were heated for 60 min at 60°C to help cyclododecane sublimation, and then to 90°C for 20 min for final drying.

2.2. Sample characterization

Micro-Raman (μ-Raman) measurements were carried out on FLG and GBD transferred onto Si/SiO_2 substrates by HORIBA Scientific LabRAM HR Evolution Raman spectrometer equipped with an integrated Olympus BX41 microscope and a laser-source at 532 nm. A laser power < 1mW was focused on a 0.7 μm wide spot on the sample surface using a 100× objective minimizing sample heating and possible damages. Atomic force microscopy (AFM) measurements were carried out in air by AIST-NT SPM AFM microscope working in tapping mode and using commercial Si probe with spring constant $k = 1.8 \div 13$ Nm^{-1} and oscillation frequency from 110 to 220 kHz. Optical transmittance spectrum of the FLG/GBD stack transferred on quartz was acquired with UV-vis-NIR PerkinElmer LAMBDA 950 spectrophotometer. The work function (Wf) evaluation of FLG has been carried on through the Kelvin probe technique using an SKP5050 Scanning Kelvin probe (KP Technology), a

contactless and non-destructive vibrating capacitor device used to measure Wf of conducting materials or surface potential of semiconducting or insulating surfaces. The instrument measures a potential gradient, termed the contact potential difference (CPD) related to the Wf difference between the sample and the reference tip of the instrument. It was possible to perform 2D scanning of the surface. A 0.286 mm scanning step was used. The sheet resistances of the two layers were measured by four-point probe method in Van der Pauw configuration (NNPSON RESISTAGE RG-8).

2.3. Solar cell fabrication

Polished Si substrates ([100]-oriented, n-doped, 1 Ω cm), with thermally grown SiO_2 layer (300 nm) were patterned by photolithography and wet-etching of the oxide (by hydrofluoric acid solution) to prepare square windows with an active area of 0.09 cm^2. The front and back contacts were realized by evaporating Ti/Au on the SiO_2 and a Ti/Pd/Ag trilayer on the back side of the n-Si, respectively. [19] Before the transfer of the graphene-based films, HF was used to remove native Si oxide from active area of the cell. The graphene-based films were transferred onto the cells by scooping the floating films kept in DI water after the rinsing process (last step of the Cu etching process). SBSCs with two configurations were fabricated to study the effects of GBD interlayer in the cell architecture: (i) reference cell with FLG as top conductive electrode (FLG/n-Si); (ii) cell with a GBD interlayer (FLG/GBD/n-Si). Unlike the top graphene that entirely covered the Au/Ti front electrode, the GBD was removed from the Au electrode and covered only the active area. The device schematics is reported in **Figure 1**. A control cell with a double GBD interlayer (*i.e.,* two GBD film transferred sequentially) was also fabricated to verify the effect of the GBD thickness on the device performance. Molecular doping was performed by exposing the top part of the cells to HNO_3 vapor (from a 70 % solution diluted 1:1 in deionized water) at room temperature for 3 min. [58]

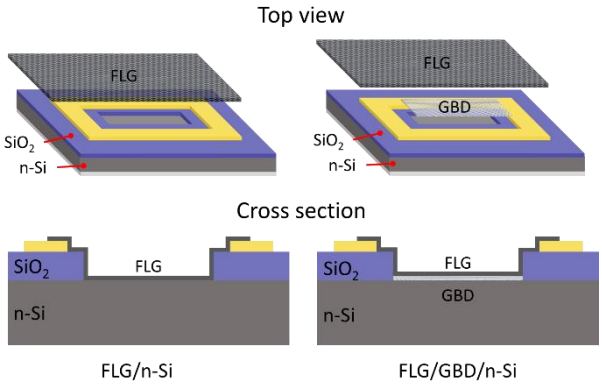

Figure 1. Schematic illustration of the fabricated devices left, reference solar cell based on FLG/n-Si junction (FLG/n-Si), right, solar cell with single GBD between single FLG and n-Si (FLG/GBD/n-Si).

2.4. Solar cell characterization

The solar cells were characterized by external quantum efficiency (EQE) and current density–voltage (J-V) measurements. EQE measurements were carried out without and with an appropriate white-light bias (optical bias, OB) to bring the cell close to the operation condition with a Bentham PVE300 apparatus (Reading, U.K.) calibrated with a Si detector and using a probe light with a spot size much smaller than the cell area. Illuminated J-V characteristics were performed with a Keithley 228a voltage/current source (Keithley Instruments Inc., Cleveland, USA) and HP 3478A multimeter measure unit (Palo Alto, USA). White light illumination was provided by a class AAA solar simulator from WACOM (model WXS- 155S-L2) equipped with a 1000 W Xenon lamp and a 400 W Halogen lamp. The light intensity was calibrated using a mono-Si reference cell in standard test conditions (25° C, AM1.5G, 1000 W/m^2).

3. Results and discussion

3.1. Structural characterization of graphene and GBD layers

Raman spectra of the FLG and GBD films are reported in Figure 2a. Both spectra exhibit the characteristic D, G and 2D peaks, respectively at ~ 1350 cm−1, ~ 1580 cm−1, ~ 2700 cm−1. [59] D to G (I_D/I_G) and 2D to G (I_{2D}/I_G) intensity ratios are used to provide quantitative information on graphene's defect density and thickness, respectively. [59,60] The spectrum of

FLG reported in Figure 2a has $I_{2D}/I_G < 1$ and $I_D/I_G \sim 0.13$, confirming the formation of few-layer graphene [61] with low defect density [60]. The spectrum of GBD is also reported and confirms the structural characteristics of films grown in the same conditions. [44] The D, G and 2D peaks are still present, but in this case the D peak strongly intensifies and the defect-related D' peak at ~ 1620 cm^{-1} appears. [44,59,62,63]. The high value of I_D/I_G intensity ratio (~ 3.2) is typical of defective carbonaceous film. [61] A similar very sharp D peak was already observed in functionalized graphene, [64] and in hydrogenated graphene grown at 650° C by plasma-CVD. [65] Raman analysis showed that the GBD film is less crystalline on long-range, having sp^2 graphene domains with lateral size of a few tens of nm, and a high percentage of sp^3 carbons along grain boundaries. A detailed analysis on the nature of the defect in the GBD film can be found in a previous work. [44] AFM measurements performed on a FLG/GBD stack on SiO_2 give information about the thickness of each layer (**Figure 2b**). These measurements showed that the thickness of FLG and GBD are 2.2 nm and 1.1 nm, respectively. These values are compatible to 4-6 layers for FLG and 1-2 layers for GBD, in agreement with the results extracted from Raman spectroscopy. The measured thickness values take into account of the presence of water buffers between the stack and SiO_2 and between each layers of the stack. [66–68] We measured the UV-vis absorption of FLG/GBD stack transferred onto quartz substrate and the result has been compared with the absorption of graphene (**Figure 2c**). The absorption spectrum of the stack is dominated by a pronounced peak at ~ 270 nm (4.6 eV). At the same wavelength, graphene shows a peak due to electron-hole (excitonic) interactions and interband transition from the bonding to the antibonding π-states. The transmittance of the stack has the maximum value of ~ 85 % in the UV region, below 250 nm (~ 5 eV), while is ~ 80 % for 600 nm < λ < 800 nm. Wf scanning of FLG onto Si is reported in **Figure 2d**. The resulting Wf for FLG is 4.7 eV, a higher value with respect to the theoretical calculations [69] since the Cu etching process can have a slight p-doping effect on graphene. [70] The sheet resistance measured for FLG and GBD films are 0.5 and 124 kΩ/sq, respectively.

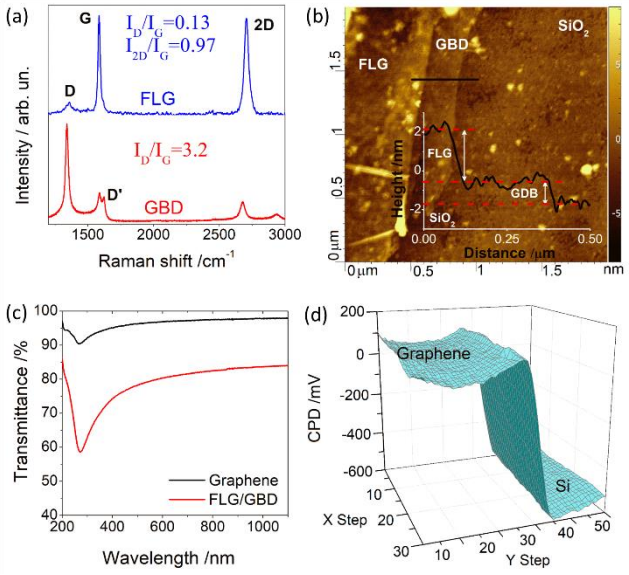

Figure 2. (a) Raman spectra of FLG and GBD, (b) AFM measurement on FLG/GBD stack on Si/SiO_2 with relative height profile, (c) transmittance of FLG/GBD stack onto quartz substrates, compared with transmittance of graphene, (d) scanning Wf of FLG onto Si substrate.

3.2. Solar cell characterization

J-V characteristic under dark condition and the corresponding ln(J)/V curves of FLG/GBD/n-Si compared with FLG/n-Si SBSC are reported in **Figure 3a**.

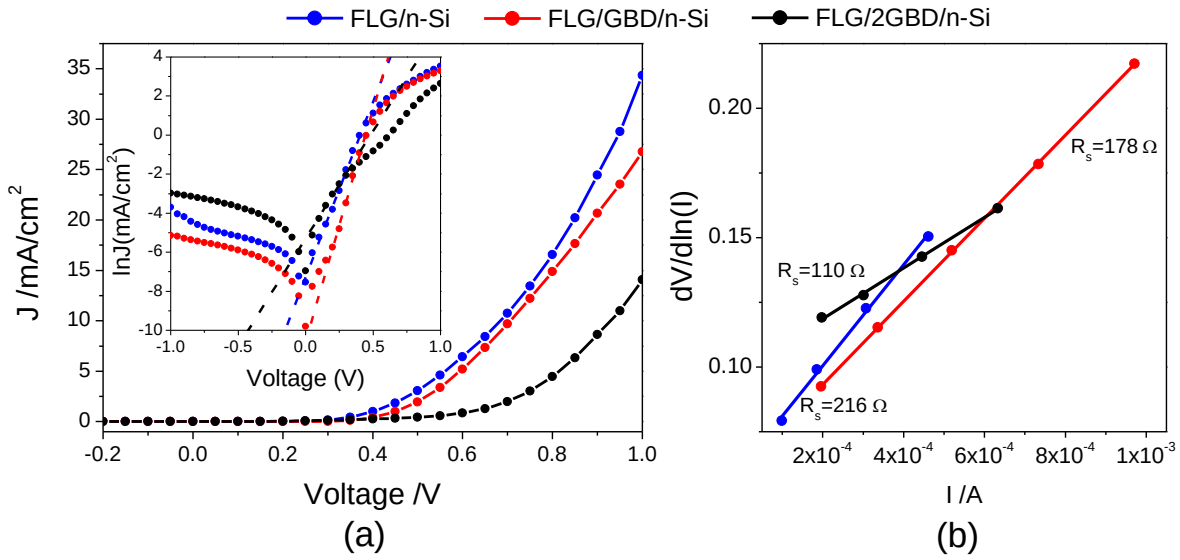

Figure 3. (a) Dark ln(J)-V characteristics with corresponding lnJ-V curves (inset) and (b) plots of dV/dln(I) versus I for FLG/n-Si (blue), FLG/GBD/n-Si (red) and FLG/2GBD/n-Si SBSCs (black curve) SBSCs.

The reverse saturation current density (J_s) is estimated to be 8.9×10^{-4} mA/cm^2 in FLG/n-Si cell, while it decreases to 4×10^{-4} mA/cm^2 in FLG/GBD/n-Si cell. This highlights that the carrier recombination is reduced thanks to the GBD interlayer in the junction. On the contrary, when adding two GBD films as interlayer (FLG/2GBD/n-Si), J_s increases to 3.8×10^{-3} mA/cm^2 indicating the presence of a large quantity of trap states among the interfaces. The series resistances R_s were extracted from the slope of the linear fitting to the curves of dV/d(lnI) ***vs*** I (**Figure 3b**). [71] R_s is reduced from 216 Ω to 178 Ω with the GBD interlayer (110 Ω in case of two GBD films). To understand the physical mechanism behind the SBSC behaviour, the band diagram of the cells is depicted in **Figure 4**.

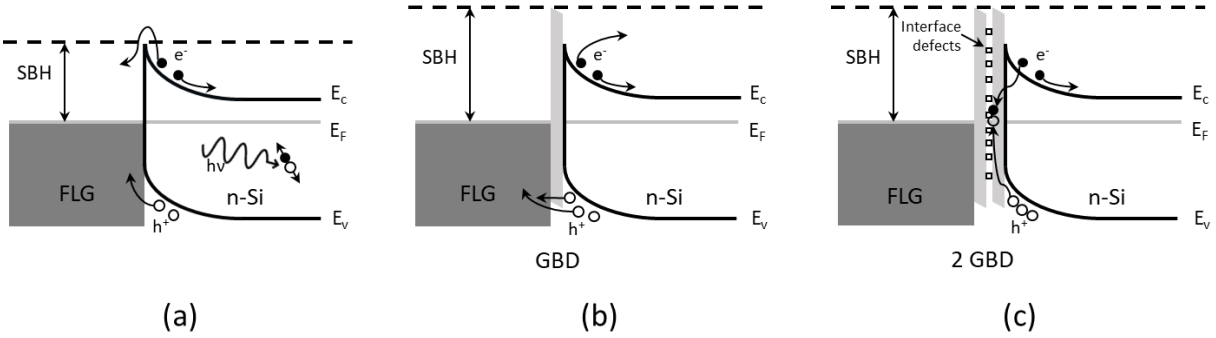

Figure 4. Schematics of band diagrams for (a) FLG/n-Si, (b) FLG/GBD/n-Si and (c) FLG/2GBD/n-Si SBSCs.

The GBD interlayer has a valance band maximum of 4.9 eV, while n-Si has the conduction band minimum and valence band maximum of 4.05 and 5.17 eV, respectively. Upon irradiation, electron−hole pairs generated in Si diffuse across FLG/n-Si interface, where they are separated by the built-in electric field of the heterojunction (**Figure 4a**). The presence of thin GBD interlayer modifies the band alignments increasing the SBH [11] (**Figure 4b**). This increase hinders the photo-generated electron transport in Si, hence reducing the leakage current. In addition, the valence band bending facilitates the photo-generated hole transport, reducing the loss due to carrier recombination. In summary, the interlayer works as an hole transport layer, while also acting as an electron blocking layer and reducing the carrier recombination at

the anode. Therefore, the interlayer lowers the saturation current density and hence increases the open circuit voltage of the device. If the interlayer thickness is doubled (as in the case of two GBD films), the probability of charge carrier tunneling lowers, causing the accumulation of holes near the interface; this results in high recombination. The recombination centers are further increased by the GBD transfer process that introduce interface defects, as already seen in graphene/h-BN/GaAs heterostructures. [29] The schematics diagram of carrier separation processes in FLG/2GBD/n-Si SBSCs is shown in Figure 4c. The analysis of the dark J-V characteristics gives information on the diode characteristics of the cells. The diode characteristics of a Schottky junction is described by thermionic emission theory of majority carriers over the Schottky barrier according to equation [14]

$$J = J_s \left[\exp\left(\frac{qV}{\eta k_B T}\right) - 1\right] \quad (1)$$

where η is the ideality factor, R_s the series resistance, k_B is Boltzmann's constant ($k=8.62\times10^{-5}$ eV/K), T is the temperature in Kelvin, q is the electronic charge (1.6×10^{-19} C) and the saturation current density J_s is described by the equation

$$J_s = A^* T^2 \exp\left(-\frac{q(SBH)}{k_B T}\right) \quad (2)$$

where A^* is the effective Richardson constant. The SBH values, evaluated by taking the slope at the forward bias linear region of ln(J)-V curve (inset of Figure 3a), are reported in **Table 1**.

Table 1. The diode characteristics of Schottky junctions reported in Figure 3

Device	SBH [eV]	η	R_s [Ω]
FLG/n-Si	0.78	2.1	216
FLG/GBD/n-Si	0.87	1.6	178
FLG/2GBD/n-Si	0.70	3.5	110

For FLG/n-Si, the SBH is estimated to be 0.78 eV, in agreement with the workfunction value measured by scanning Kelvin probe. The SBH increases when the GBD interlayer is added (0.87 eV). The η values were also extracted from ln(J)-V curve: the introduction of the

interlayer reduces η from 2.1 to 1.6, as previously reported for undoped FLG/n-Si diodes. [14] With two GBD films as interlayer, the diode curve showed a non-linearity at the lower bias. This is due to the presence of leakage currents usually attributed to generation and recombination of carriers in the charge space region, field emission and thermionic field emission or surface/edge effects that may lead to local barrier lowering. [72,73] In this case the SBH is 0.70 eV, lower than the SBH found for the other cell configurations, and η increases to 3.5. [74] Additional characterization is presented in **Figure 5**, which shows the EQE of the cells acquired with and without OB.

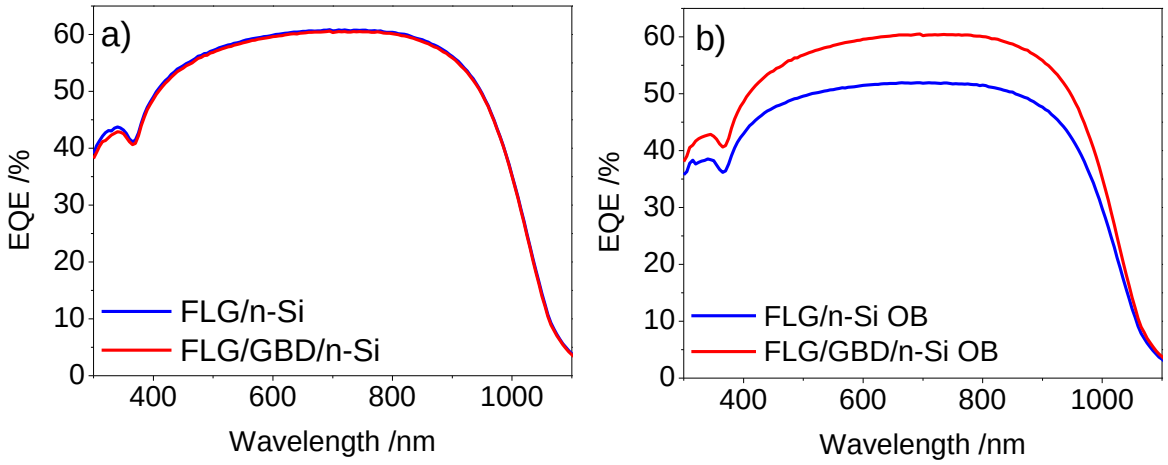

Figure 5. EQE curves without (a) and with (b) OB of G /n-Si (blue) and FLG/GBD/n-Si (red) SBSCs.

The EQE curves acquired without OB are identical for the two cells (**Figure 5a**). They reach a value of ~60 % in the wavelength range 600 nm < λ < 800 nm, in line with state-of-the-art Si solar cells. [14] Evaluating EQE with OB, the cells show a different behavior: FLG/GBD/n-Si shows an unchanged EQE curve with maximum efficiency at ~ 60 %, while FLG/n-Si shows a low efficiency of ~ 50% (**Figure 5b**). This result indicates that the introduction of the GBD interlayer significantly improves the electron-hole pair separation and collection by the corresponding electrodes. Since the photogeneration for the device without and with the interlayer is identical, the higher EQE observed with the GBD is due to more efficient charge

separation and charge collection as a result of increased SBH and reduced recombination centers at the interfaces.

3.3. Doping treatment

Doping treatment can induce modification in the graphene lattice, resulting in an effect on the vibrational modes probed by Raman spectroscopy. [54,59] It is possible to obtain information about carriers concentration and strain by evaluating the G and 2D bands frequency. [75–77] FLG layer after doping was largely discussed in previous work, confirming a p-doping with a doping level of ~ 2×10^{13} cm^{-2}. [78] To evaluate the effects of doping on GBD, the correlation between the Raman shift of the G and 2D band was studied. [77] Points in the map in **Figure 6** corrispond to Raman spectra acquired on the GBD films transferred on Si/SiO_2, before and after the doping treatment. The points are located between two axes that describe the pure strain with a slope of 2.45 [76] (solid black line in Figure 6) and the pure doping with a slope of 0.7 [75] (solid gray line in Figure 6). The origin of this coordinate system (1582 cm^{-1}, 2670 cm^{-1}) corresponds to undoped and unstrained graphene for excitation energy equal to 2.33 eV. [79] The point distribution in the map is due to in-homogeneity of the sample but it was possible to extimate doping and strain evaluating the center of point cluster. [79]

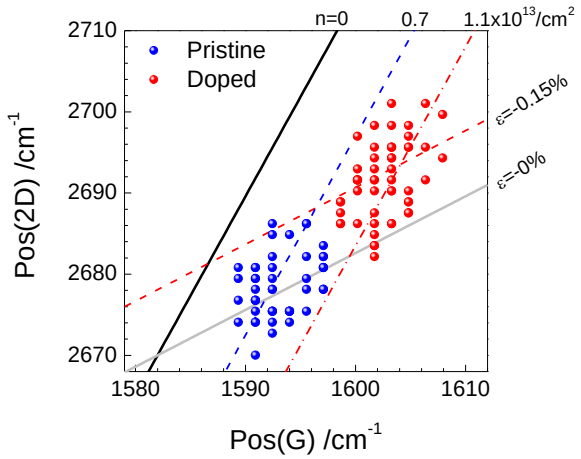

Figure 6. G-2D Correlation map for GBD layer. The solid black line and the solid gray line represent the pure strain and pure doping, respectively. The dashed line represent the projection on strain and doping axes.

Pristine GBD appears characterized by an intrinsic doping of ~ 0.7 × 10^{13} cm^{-2} due to the different nature of GBD in respect the pristine graphene. After doping treatment, the point distribution moves to a compressive strain of -0.15% and doping of ~ 1.1 × 10^{13} cm^{-2}. This result shows that the doping treatment works differently on the two layers, with a less significant doping on GBD. The J-V characteristics under illumination were acquired on FLG/GBD/n-Si with best EQE performance. The curves were acquired before and after the doping treatment with HNO_3.[19] The effect of the doping treatments on FLG/GBD/n-Si J-V curves is reported in **Figure 7** and the photovoltaics parameters are summarized in **Table 2**.

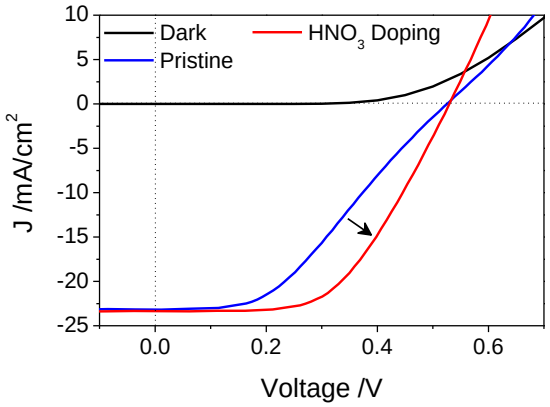

Figure 7. J-V curve of FLG/GBD/n-Si under illumination in standard condition, before and after doping treatment with HNO_3

Table 2. Photovoltaic parameters calculated from curves reported in Figure 7 for FLG/GBD/n-Si SBSC

Process step	Jsc [mA/cm²]	Voc [V]	FF [%]	PCE [%]	Rs [Ω]
Pristine	23.1	0.52	39.4	4.8	17.5
Doped HNO3 3min	23.3	0.53	54.2	6.7	7.8

The pristine cell under illumination shows good photovoltaic characteristics with short circuit current density (J_{sc}), open circuit voltage (V_{oc}), fill factor (FF), PCE and series resistance of 23.1 mA/cm^2, 0.52 V, 39.4 %, 4.8 %, 17.5 Ω, respectively. The molecular doping improves the cell performance in particular in term of PCE and FF, while reducing the Rs: The FF increases to 54.2 % and consequently the PCE reaches 6.7 %, while the R_s decreases to 7.8 Ω. The

influence of doping on the short-circuit current density (J_{sc}) is negligible, as already observed in literature. [15,78] The improvement in the cell photovoltaic parameters by HNO_3 treatment can be attributed to different factors. The molecular doping is expected to decrease the sheet resistance of graphene [15,18] and this leads to a proportional decrease in the R_s of the solar cell, and to a concomitant increase in the FF. Beside the significant decrease in the graphene sheet resistance, a volatile oxidant treatment such as the exposure to HNO_3 vapor is expected to improve the uniformity of the Schottky junction by saturating defects at the interfaces. This should also contribute to decrease the cell Rs, further increasing its FF. [15] The effects of ageing on the doping treatment and on the cell performance were also investigated. The long-term stability of solar cells is a very important factor in view of commercialization. [80] As reported in our previous work on a FLG/n-Si SBSC, ageing leads to the degradation of the Voc and FF parameters and to the increase of "the S shape" of the IV curve. [19] This effect was due to the instability of graphene doping by volatile compounds (HNO_3), which lowered the SBH and hence decreased the value of V_{oc}. [15,20] After three weeks of storage in air, the final effect on PCE was a 70% reduction with respect to the freshly doped cell, but a complete recovery was possible upon repeating the doping procedure by exposure to HNO_3 vapors. A similar degradation and recovery behaviour was observed in the present study on FLG/GBD/n-Si SBSC.

4. Conclusion

The role of a graphene-based derivative as interfacial layer in Schottky barrier solar cell made with few-layer graphene and n-Si was evaluated. J-V curves and external quantum efficiency measurements confirm that the GBD interlayer reduces charge traps, added by interface states and recombination centers. It ultimately leads to a decrease of the saturation current and series resistance, bringing the Schottky barrier height from 0.78 to 0.87 V. The ideality factor is also reduced from 2.1 to 1.6, demonstrating the reduction of interface recombination processes.

These improvements derived by the insertion of a GBD interlayer in the FLG/n-Si junction, were confirmed by the ~ 20% increase in external quantum efficiency (measured under white-light bias to keeping the cell closer to the operation condition). The insertion of a GBD interlayer with doubled thickness (made by sequentially transferring two GBD films) results in charge accumulation at the interface, acting as detrimental recombination centers. This proves that the GBD film has intrinsically an optimal thickness (~ 1.1 nm) to work as hole transport layer in this cell architecture, as in the case of organic solar cells. The effect of a doping treatment by HNO_3 vapour on the cell was also investigated and proved an improvement of all photovoltaic parameters, raising the power conversion efficiency from 4.8 % up to 6.7 %. This work sets the basis for the exploration of Si Schottky-barrier solar cells fabricated with graphene-based films with selected properties (*e.g.*, such as layer number, workfunction, charge transport behaviour, doping level, etc.) and in different configurations, towards improved cell performance.

Acknowledgements

((Acknowledgements, general annotations, funding. Other references to the title/authors can also appear here, such as “Author 1 and Author 2 contributed equally to this work.”))

Received: ((will be filled in by the editorial staff))
Revised: ((will be filled in by the editorial staff))
Published online: ((will be filled in by the editorial staff))

REFERENCES

[1] K. S. Novoselov, A. Mishchenko, A. Carvalho, A. H. Castro Neto, *Science (80-.).* **2016**, *353*.

[2] L. Xinming, Z. Hongwei, W. Kunlin, C. Anyuan, W. Jinquan, L. Chunyan, J. Yi, L. Zhen, L. Xiao, W. Dehai, *Adv. Mater.* **2010**, *22*, 2743.

[3] K. Ihm, J. T. Lim, K.-J. Lee, J. W. Kwon, T.-H. Kang, S. Chung, S. Bae, J. H. Kim, B. H. Hong, G. Y. Yeom, *Appl. Phys. Lett.* **2010**, *97*, 32113.

[4] Y. Ye, L. Dai, *J. Mater. Chem.* **2012**, *22*, 24224.

[5] X. An, F. Liu, S. Kar, *Carbon N. Y.* **2013**, *57*, 329.

[6] X. Yu, L. Yang, Q. Lv, M. Xu, H. Chen, D. Yang, *Nanoscale* **2015**, *7*, 7072.

[7] E. Singh, H. S. Nalwa, *J. Nanosci. Nanotechnol.* **n.d.**, *15*, 6237.

[8] Y. Lin, X. Li, D. Xie, T. Feng, Y. Chen, R. Song, H. Tian, T. Ren, M. Zhong, K. Wang, H. Zhu, *Energy Environ. Sci.* **2013**, *6*, 108.

[9] L. Tao, Z. Chen, X. Li, K. Yan, J.-B. Xu, *npj 2D Mater. Appl.* **2017**, *1*, 19.

[10] L. Xinming, Z. Miao, D. Mingde, L. Zheng, Z. Li, L. Yuanchang, Y. Yao, Y. Tingting, L. Xiao, W. Kunlin, Z. Hongwei, F. Ying, *Small* **2015**, *12*, 595.

[11] Y. Song, X. Li, C. Mackin, X. Zhang, W. Fang, T. Palacios, H. Zhu, J. Kong, *Nano Lett.* **2015**, *15*, 2104.

[12] L. Xinming, X. Dan, P. Hyesung, Z. T. Helen, W. Kunlin, W. Jinquan, Z. Minlin, W. Dehai, K. Jing, Z. Hongwei, *Adv. Energy Mater.* **2013**, *3*, 1029.

[13] Y. F. Li, W. Yang, Z. Q. Tu, Z. C. Liu, F. Yang, L. Q. Zhang, R. Hatakeyama, *Appl. Phys. Lett.* **2014**, *104*, 43903.

[14] X. Miao, S. Tongay, M. K. Petterson, K. Berke, A. G. Rinzler, B. R. Appleton, A. F. Hebard, *Nano Lett.* **2012**, *12*, 2745.

[15] T. Cui, R. Lv, Z.-H. Huang, S. Chen, Z. Zhang, X. Gan, Y. Jia, X. Li, K. Wang, D. Wu, F. Kang, *J. Mater. Chem. A* **2013**, *1*, 5736.

[16] X. Zhang, C. Xie, J. Jie, X. Zhang, Y. Wu, W. Zhang, *J. Mater. Chem. A* **2013**, *1*, 6593.

[17] C. Xie, X. Zhang, K. Ruan, Z. Shao, S. S. Dhaliwal, L. Wang, Q. Zhang, X. Zhang, J. Jie, *J. Mater. Chem. A* **2013**, *1*, 15348.

[18] X. Li, D. Xie, H. Park, M. Zhu, T. H. Zeng, K. Wang, J. Wei, D. Wu, J. Kong, H. Zhu, *Nanoscale* **2013**, *5*, 1945.

[19] L. Lancellotti, E. Bobeico, A. Capasso, E. Lago, P. Delli Veneri, E. Leoni, F. Buonocore, N. Lisi, *Sol. Energy* **2016**, *127*, 198.

[20] E. Shi, H. Li, L. Yang, L. Zhang, Z. Li, P. Li, Y. Shang, S. Wu, X. Li, J. Wei, K. Wang, H. Zhu, D. Wu, Y. Fang, A. Cao, *Nano Lett.* **2013**, *13*, 1776.

[21] T. Feng, D. Xie, Y. Lin, Y. Zang, T. Ren, R. Song, H. Zhao, H. Tian, X. Li, H. Zhu, L. Liu, *Appl. Phys. Lett.* **2011**, *99*, 233505.

[22] D. Xu, X. Yu, L. Zuo, D. Yang, *RSC Adv.* **2015**, *5*, 46480.

[23] L. Yang, X. Yu, M. Xu, H. Chen, D. Yang, *J. Mater. Chem. A* **2014**, *2*, 16877.

[24] Y. Tsuboi, F. Wang, D. Kozawa, K. Funahashi, S. Mouri, Y. Miyauchi, T. Takenobu, K. Matsuda, *Nanoscale* **2015**, *7*, 14476.

[25] M. F. Bhopal, K. Akbar, M. A. Rehman, D. won Lee, A. ur Rehman, Y. Seo, S.-H. Chun, S. H. Lee, *Carbon N. Y.* **2017**, *125*, 56.

[26] A. Alnuaimi, I. Almansouri, I. Saadat, A. Nayfeh, *Sol. Energy* **2018**, *164*, 174.

[27] W. Jie, F. Zheng, J. Hao, *Appl. Phys. Lett.* **2013**, *103*, 233111.

[28] X. Li, W. Chen, S. Zhang, Z. Wu, P. Wang, Z. Xu, H. Chen, W. Yin, H. Zhong, S. Lin, *Nano Energy* **2015**, *16*, 310.

[29] X. Li, S. Lin, X. Lin, Z. Xu, P. Wang, S. Zhang, H. Zhong, W. Xu, Z. Wu, W. Fang, *Opt. Express* **2016**, *24*, 134.

[30] H. He, X. Yu, Y. Wu, X. Mu, H. Zhu, S. Yuan, D. Yang, *Nano Energy* **2015**, *16*, 91.

[31] P. Wang, X. Li, Z. Xu, Z. Wu, S. Zhang, W. Xu, H. Zhong, H. Chen, E. Li, J. Luo, Q.

Yu, S. Lin, *Nano Energy* **2015**, *13*, 509.

[32] S. Lin, X. Li, S. Zhang, P. Wang, Z. Xu, H. Zhong, Z. Wu, H. Chen, *Appl. Phys. Lett.* **2015**, *107*, 191106.

[33] N. E. Gorji, *Phys. E Low-dimensional Syst. Nanostructures* **2015**, *70*, 84.

[34] J. Liang, H. Bi, D. Wan, F. Huang, *Adv. Funct. Mater.* **2012**, *22*, 1267.

[35] H. Bi, F. Huang, J. Liang, X. Xie, M. Jiang, *Adv. Mater.* **2011**, *23*, 3202.

[36] M. A. Rehman, I. Akhtar, W. Choi, K. Akbar, A. Farooq, S. Hussain, M. A. Shehzad, S.-H. Chun, J. Jung, Y. Seo, *Carbon N. Y.* **2018**, *132*, 157.

[37] J. Ma, H. Bai, W. Zhao, Y. Yuan, K. Zhang, *Sol. Energy* **2018**, *160*, 76.

[38] J.-H. Meng, X. Liu, X.-W. Zhang, Y. Zhang, H.-L. Wang, Z.-G. Yin, Y.-Z. Zhang, H. Liu, J.-B. You, H. Yan, *Nano Energy* **2016**, *28*, 44.

[39] L. Lancellotti, L. Sansone, E. Bobeico, E. Lago, M. D. Noce, P. D. Veneri, A. Borriello, M. Casalino, G. Coppola, M. Giordano, M. Iodice, in *2015 Fotonica AEIT Ital. Conf. Photonics Technol.*, **2015**, pp. 1–4.

[40] N. Balis, E. Stratakis, E. Kymakis, *Mater. Today* **2016**, *19*, 580.

[41] E. Kymakis, M. M. Stylianakis, G. D. Spyropoulos, E. Stratakis, E. Koudoumas, C. Fotakis, *Sol. Energy Mater. Sol. Cells* **2012**, *96*, 298.

[42] A. Capasso, L. Salamandra, A. Di Carlo, J. M. Bell, N. Motta, *Beilstein J. Nanotechnol.* **2012**, *3*, 524.

[43] A. Capasso, L. Salamandra, A. Chou, A. Di Carlo, N. Motta, *Sol. Energy Mater. Sol. Cells* **2014**, *122*, 297.

[44] A. Capasso, L. Salamandra, G. Faggio, T. Dikonimos, F. Buonocore, V. Morandi, L. Ortolani, N. Lisi, *ACS Appl. Mater. Interfaces* **2016**, *8*, 23844.

[45] A. Capasso, F. Matteocci, N. Leyla, M. Prato, J. Buha, L. Cinà, V. Pellegrini, A. Di Carlo, F. Bonaccorso, *Adv. Energy Mater.* **2016**, *6*, 1600920.

[46] Q. Van Le, J.-Y. Choi, S. Y. Kim, *FlatChem* **2017**, *2*, 54.

[47] J. Bouclé, N. Herlin-Boime, *Synth. Met.* **2016**, *222*, 3.

[48] M. Pumera, C. H. A. Wong, *Chem. Soc. Rev.* **2013**, *42*, 5987.

[49] J. O. Sofo, A. S. Chaudhari, G. D. Barber, *Phys. Rev. B* **2007**, *75*, 153401.

[50] F. Buonocore, A. Capasso, N. Lisi, *J. Chem. Phys.* **2017**, *147*, 104705.

[51] F. Buonocore, A. Capasso, N. Lisi, *Mater. Res. Express* **2014**, *1*, 15608.

[52] Q. Etienne, F. Roux, F. Emieux, P. Faucherand, E. Kymakis, G. Volonakis, F. Giustino, B. Martín-García, I. Moreels, S. A. Gürsel, A. B. Yurtcan, V. Di Noto, A. Talyzin, I. Baburin, D. Tranca, G. Seifert, L. Crema, G. Speranza, V. Tozzini, P. Bondavalli, G. Pognon, C. Botas, D. Carriazo, G. Singh, T. Rojo, G. Kim, W. Yu, C. P. Grey, V. Pellegrini, *2D Mater.* **2015**, *2*, 30204.

[53] S. Santangelo, G. Messina, A. Malara, N. Lisi, T. Dikonimos, A. Capasso, L. Ortolani, V. Morandi, G. Faggio, *Diam. Relat. Mater.* **2014**, *41*, 73.

[54] A. Capasso, T. Dikonimos, F. Sarto, A. Tamburrano, G. De Bellis, M. S. Sarto, G. Faggio, A. Malara, G. Messina, N. Lisi, *Beilstein J. Nanotechnol.* **2015**, *6*, 2028.

[55] A. Capasso, M. De Francesco, E. Leoni, T. Dikonimos, F. Buonocore, L. Lancellotti, E. Bobeico, M. S. Sarto, A. Tamburrano, G. De Bellis, N. Lisi, *Appl. Phys. Lett.* **2014**, *105*, 113101.

[56] G. Faggio, A. Capasso, G. Messina, S. Santangelo, T. Dikonimos, S. Gagliardi, R. Giorgi, V. Morandi, L. Ortolani, N. Lisi, *J. Phys. Chem. C* **2013**, *117*, 21569.

[57] N. Lisi, T. Dikonimos, F. Buonocore, M. Pittori, R. Mazzaro, R. Rizzoli, S. Marras, A. Capasso, *Sci. Rep.* **2017**, *7*, 9927.

[58] L. Lancellotti, E. Bobeico, A. Capasso, M. Della Noce, T. Dikonimos, N. Lisi, P. D. Veneri, in *2014 Fotonica AEIT Ital. Conf. Photonics Technol.*, **2014**, pp. 1–3.

[59] A. C. Ferrari, J. C. Meyer, V. Scardaci, C. Casiraghi, M. Lazzeri, F. Mauri, S. Piscanec, D. Jiang, K. S. Novoselov, S. Roth, A. K. Geim, *Phys. Rev. Lett.* **2006**, *97*, 187401.

[60] M. A. Pimenta, G. Dresselhaus, M. S. Dresselhaus, L. G. Cancado, A. Jorio, R. Saito,

Phys. Chem. Chem. Phys. **2007**, *9*, 1276.

[61] A. C. Ferrari, *Solid State Commun.* **2007**, *143*, 47.

[62] L. M. Malard, M. A. Pimenta, G. Dresselhaus, M. S. Dresselhaus, *Phys. Rep.* **2009**, *473*, 51.

[63] N. Lisi, F. Buonocore, T. Dikonimos, E. Leoni, G. Faggio, G. Messina, V. Morandi, L. Ortolani, A. Capasso, *Thin Solid Films* **2014**, *571*, 139.

[64] M. Seifert, J. E. B. Vargas, M. Bobinger, M. Sachsenhauser, A. W. Cummings, S. Roche, J. A. Garrido, *2D Mater.* **2015**, *2*, 24008.

[65] Y. Wang, X. Xu, J. Lu, M. Lin, Q. Bao, B. Özyilmaz, K. P. Loh, *ACS Nano* **2010**, *4*, 6146.

[66] K. Jinkins, J. Camacho, L. Farina, Y. Wu, *Appl. Phys. Lett.* **2015**, *107*, 243107.

[67] P. Nemes-Incze, Z. Osváth, K. Kamarás, L. P. Biró, *Carbon N. Y.* **2008**, *46*, 1435.

[68] W. Jung, J. Park, T. Yoon, T.-S. Kim, S. Kim, C.-S. Han, *Small* **2014**, *10*, 1704.

[69] O. L. and B. P. and F. M. P. and A. V. and C. Van Haesendonck, *J. Phys. Condens. Matter* **2017**, *29*, 35003.

[70] M. Wang, E. H. Yang, R. Vajtai, J. Kono, P. M. Ajayan, *J. Appl. Phys.* **2018**, *123*, 195103.

[71] A. Di Bartolomeo, G. Luongo, F. Giubileo, N. Funicello, G. Niu, T. Schroeder, M. Lisker, G. Lupina, *2D Mater.* **2017**, *4*, 25075.

[72] R. T. Tung, *Mater. Sci. Eng. R Reports* **2001**, *35*, 1.

[73] R. T. Tung, *Appl. Phys. Rev.* **2014**, *1*, 11304.

[74] J. H. Werner, H. H. Güttler, *J. Appl. Phys.* **1991**, *69*, 1522.

[75] A. Das, S. Pisana, B. Chakraborty, S. Piscanec, S. K. Saha, U. V Waghmare, K. S. Novoselov, H. R. Krishnamurthy, A. K. Geim, A. C. Ferrari, A. K. Sood, *Nat. Nanotechnol.* **2008**, *3*, 210.

[76] J. Zabel, R. R. Nair, A. Ott, T. Georgiou, A. K. Geim, K. S. Novoselov, C. Casiraghi,

Nano Lett. **2012**, *12*, 617.

[77] J. E. Lee, G. Ahn, J. Shim, Y. S. Lee, S. Ryu, *Nat. Commun.* **2012**, *3*, 1024.

[78] L. Lancellotti, E. Bobeico, A. Castaldo, P. Delli Veneri, E. Lago, N. Lisi, *Thin Solid Films* **2018**, *646*, 21.

[79] T. G. A. Verhagen, K. Drogowska, M. Kalbac, J. Vejpravova, *Phys. Rev. B* **2015**, *92*, 125437.

[80] E. Singh, H. S. Nalwa, *RSC Adv.* **2015**, *5*, 73575.